



Full Length Article

Magnonic ballistic transport across Fe-Ni alloy nanojunctions between Fe/Co leads using Phase Field Matching and Ising Effective Field Theory approaches

Elie A. Moujaes^{a,*}, A. Khater^{b,e}, M. Abou Ghantous^c, V. Ashokan^d

^a Departamento de Física, Universidade Federal de Rondônia, 76900-900 Porto Velho, Brazil

^b Department of Physics, Université du Maine, Le Mans 72085, France

^c Science Department, American University of Technology, Fidar Campus, Halat, Lebanon

^d Department of Physics, Dr. B. R. Ambedkar National Institute of Technology, Jalandhar 144011, India

^e Institute of Physics, Jan Dlugosz University, Am. Armii Krajowej 13/15, Czestochowa, Poland



ARTICLE INFO

Keywords:

Ising-EFT

Ballistic transport

Phase Field Matching Theory

Landauer-Büttiker formalism

ABSTRACT

We analyze the scattering and ballistic transport of spin waves (SW) of Fe/Co leads across iron-nickel alloy nanojunctions, for different nanojunction nickel concentrations. The analytical and numerical analysis is developed for variable thicknesses n of the (100) atomic layers of the homogeneous Fe-Ni alloy nanojunctions, where $1 \leq n \leq 7$. The ordered magnetic states are treated in the virtual crystal approximation (VCA) and computed using the Ising EFT-MFT method. The spin dynamics and the SW scattering at the nanojunctions are examined by implementing the phase field matching theory (PFMT) for the Heisenberg Hamiltonian. Ballistic coherent reflection and transmission probabilities of the SWs incident from the Fe/Co leads onto the nanojunctions, are calculated using the Landauer-Büttiker formalism. Resonance assisted maxima of the ballistic SW transmission spectra are also along various directions of the Brillouin zone. The characteristics of these maxima can be modified by varying several factors including the nanojunction thickness, the number of layers, the propagation path, the alloy concentrations and temperature.

1. Introduction

The tremendous research effort to understand and manipulate the properties of magnetic nanomaterials is stimulated by the objective to enhance the performance of physical devices using these materials as their constitutive elements. In particular, nanostructures of magnetic materials, with specifically required properties, are urgently needed to design more advanced devices for information processing and storage, energy applications, and permanent magnets [1–3]. The discovery of new types of magnetic nanostructures, whose behavior is often very different from that of bulk, has also revealed new aspects of known phenomena, and led to important progress in the fields of spin wave magnonics [4,5], and spin-based electronics [6].

Equally spin wave excitations have attracted increasingly great attention, and are used and analyzed in several areas, ranging from spin-polarized scanning tunneling microscopy [7] to modelling the magnonic coherent transport for systems of interest via atomic contacts and nano scale junctions [8–12]. Recently the experimental research in magnonics concentrates primarily on the study of magnetic systems and the transport properties of their SWs, at the microscopic scale [13]. However,

despite the compelling attempts dedicated to this growing field, the experimental work for the emission and detection of short-wavelength SWs at the nano scale is limited and continues to be a key challenge [14,15].

Several types of nanomaterials are being studied to obtain optimum characteristics for the efficiency of the magnetic devices. In this respect, it is well known that the use of magnetic transition metals (TM) to prepare bimetallic multilayers has been a successful approach to modulate and control the magnetic properties of such nanomaterial systems. Hence, one can expect that magnetic nanostructures of TM alloys can be of significant interest. The investigation of the magnonic ballistic transport across homogeneous TM alloy nanostructures has therefore been initiated recently with this target, in particular to identify the magnetic ground states of the Fe-Co alloy nanojunctions [16,17], using a combination of Ising Effective field theory (EFT) and Mean field theory (MFT) methods. The same authors also computed the magnonic ballistic transport across such nanojunctions [8–10,18], employing the theoretical PFMT method.

In the present paper, we give an extensive analysis of the magnonic ballistic transport across the $[\text{Fe}_{1-c}\text{Ni}_c]_n$ homogeneous alloy nanojunctions between Fe/Co leads, where n is the number of the [100] atomic

* Corresponding author.

E-mail address: eamoujaes@unir.br (E.A. Moujaes).

layers of the nanojunction. This work is motivated by the fact that the iron-nickel alloys present a rich phenomenology [20], and a complex phase diagram [21], allowing them to be produced at the nano scale by a variety of techniques, via mechanical alloying [22], thermal evaporation [23], electrodeposition [24], or even metal-plasma reaction [25].

Due to their unique low coefficient of thermal expansion, Fe-Ni alloys have been used in industrial applications for over 100 years [20,22–25] including thermostatic bimetals, glass sealing, integrated circuit packaging, cathode ray shadow masks, membranes for liquid natural gas tankers, read-write heads for magnetic storage, magnetic shielding and high performance transformer cores amongst many others. In particular Fe-Ni alloys with $0.29 \leq c \leq 0.36$ can be used for measuring instruments requiring magnetic temperature compensation [26]. Alloys with higher Ni concentrations such as $\text{Fe}_{0.19}\text{Ni}_{0.81}$, known as the *permalloy* are commonly used in motor cases, and in magnetic resonance tomography shield covers as well as a model system to analyze the effects of nanostructuring on the symmetry and dynamics of domain walls [27]; on the other hand, alloys such as $\text{Fe}_{0.5}\text{Ni}_{0.5}$ with 50 % Ni, possess a Pt-like high catalytic activity [28].

Nowadays experimental research is focusing on the study of interdiffusion in nanometric Fe-Ni multilayer films [29]. For instance, magnetic transport properties of Fe/SiO₂/Ni multilayers grown on Si/SiO₂ substrates have revealed a predominant contribution of anisotropic magnetic resistance both at room and low temperatures [30]. Multilayers of Fe/Ni have been thoroughly studied and it has been confirmed that their magnetic properties depend both on individual layer thickness and the ratio of the constituents [31]; thus investigating the effect of piling up more layers could be an improvement by influencing the performance of the nanojunction device. Up to our knowledge, no theoretical work has been devoted to examine Fe-Ni nanojunctions coupled to transition metal leads.

The Fe and Ni bulk metals are both ferromagnetic, with characteristic Curie temperatures of $\sim 1050\text{K}$ and 631K respectively. In a previous work, several TM bulk metals were considered, including Fe and Ni, to calculate their corresponding magnetic exchange constants and magnetizations in the ordered phase, [32], by applying the Ising effective field theory (EFT) [33–36], within a nearest neighbour exchange interaction formalism.

Here we will assume that the Fe-Ni bulk alloys have a clear bcc structure for $c \leq 0.25$, and, in contrast, a clear fcc structure for $c \geq 0.6$ thus avoiding the invar region (close to $c = 0.35$) [19] at which some anomalies of the physical properties might take place. The Fe-Fe, Ni-Ni, and Fe-Ni exchange constants (J) were calculated by analytical means making use of the virtual crystal approximation (VCA).

The model computations for the spin dynamics in the nanojunction systems, the SW scattering at the nanojunctions, and the magnonic ballistic transport, are developed using the Heisenberg Hamiltonian representation of the magnetic ground states of the systems, and employing the phase field matching theory (PFMT) [8–10,18] based on the appropriate phase matching of the Bloch states of the leads to the localized states in the nanojunction scattering region. The PFMT method, equivalent to the non-equilibrium Greens function method but more transparent, was developed as an imperative tool [18,37–41] to solve the scattering problems of elementary excitations, notably magnons, phonons, and electrons, across nanostructures and molecular junctions. It thus yields the Landauer-Büttiker, [42,43], reflection R and transmission T probabilities for the SW incident from the leads onto the nanojunction systems.

The layout of the paper is as follows. Section 2.1 presents a brief presentation of the method used to calculate the Fe-Fe, Ni-Ni, and Fe-Ni exchange constants using the Ising effective field theory (EFT) and the virtual crystal approximation for the alloys $\text{Fe}_{1-c}\text{Ni}_c$; this method proves to be more suitable and accurate than the one used in a previous work [47]. The model calculations for the spin dynamics, designed to obtain the localized spin states at the magnetic nanojunction and their dispersion using the PFMT, are presented and discussed in Section 2.2.

Section 3 contains expressions of the sublattice magnetization for the Ni and Fe sites as well as the total magnetization per layer of the nanojunctions. Section 4 gives a brief analysis of the Landauer-Büttiker scattering problem for SWs incident from the Fe/Co leads onto the nanojunction layers. General results including magnon coherent transport at the nanojunctions along various incident directions and at different temperatures, are presented and discussed in Section 5, and are applied for Ni alloy concentrations $c = 0.08, 0.13, 0.16$ (bcc nanojunctions) and $0.65, 0.81$ (fcc nanojunctions) with thicknesses $1 \leq n \leq 7$. The reason behind choosing these specific c values is the availability of reliable experimental parameters needed to extract J for further computations and, as was mentioned before, to avoid concentrations belonging to the invar region. Finally a summary of what was achieved in this work is found in Section 6.

2. Theoretical model for spin dynamics

Fig. (1)(a)-(b) gives a schematic representation of four and seven layered fcc and bcc systems respectively showing the symmetry adopted. In both cases the atomic layers of pure Fe/Co atoms at the nanojunction extremities are the limits of the Fe/Co leads on the left and on the right (orange spheres) of the nanojunction. The sites in the homogeneous alloy nanojunction itself (blue spheres), are randomly distributed Ni and Fe atoms, with their corresponding concentration probabilities.

2.1. EFT-VCA method in iron - nickel alloys

The Ising effective field theory (EFT) is known to be superior to the mean field theory (MFT) [33–36], because it incorporates the contributions of the single-site spin correlations to the order parameter. We use EFT in this work, in conjunction with the virtual crystal approximation (VCA) for the homogeneous Fe-Ni alloy, to model and determine the Fe-Fe, Ni-Ni and Fe-Ni exchange constants for different Ni concentrations.

In a previous work [47], a procedure was adopted to calculate the exchange constants $J_{\text{Fe-Fe}}$, $J_{\text{Ni-Ni}}$ and $J_{\text{Fe-Ni}}$. It was based on experimental values of the stiffness constant D of the Fe-Ni alloy and on expressions of ensemble averages to compute D for the individual Fe and Ni constituents, as a first approximation. This might not be entirely correct and a better approach is in order. Therefore to be consistent with the choice of a ferromagnetic alloy, such as the Fe-Ni alloy, made up of two TM ferromagnetic elements and to avoid relying on too much experimental results gathered from different sources, we have recalculated the exchange parameters using another method that strictly depends on the results of the Ising EFT and the assumption of the VCA (discussed later) for homogeneous TM alloys. The only inevitable experimental ingredient that we must have access to is the critical temperature T_c for each concentration c .

Within the realms of this new technique, there are two steps to extract the exchange constants. In the first step we compute the alloy average value of the exchange constant $J_{\text{av}}(c)$ for different concentrations using the EFT-calculated constitutive relations [32] for bulk magnetic materials; these can be established as $R_N = k_B T_c / z J_{\text{av}} S(S+1) = 0.304$ for the bcc Fe-Ni alloy with $Z = 8$, $S = 1$ and $R_N = 0.314$, $Z = 12$ and $S = 1$ for the fcc system, k_B being the Boltzmann constant. Since $k_B T_c$ varies with c and is known experimentally for the concentrations we have chosen, [46,48], and considering the spin values for iron and nickel as $S_{\text{Fe}} = S_{\text{Ni}} = 1$, $J_{\text{av}}(c)$ can be computed via the above expressions of R_N .

It has also been shown from neutron scattering measurements in Fe-Ni alloys [49], that the value of the atomic magnetomechanical ratio for Ni and Fe does not change upon alloying, while the local magnetic moment does. This experimental evidence implies that we can

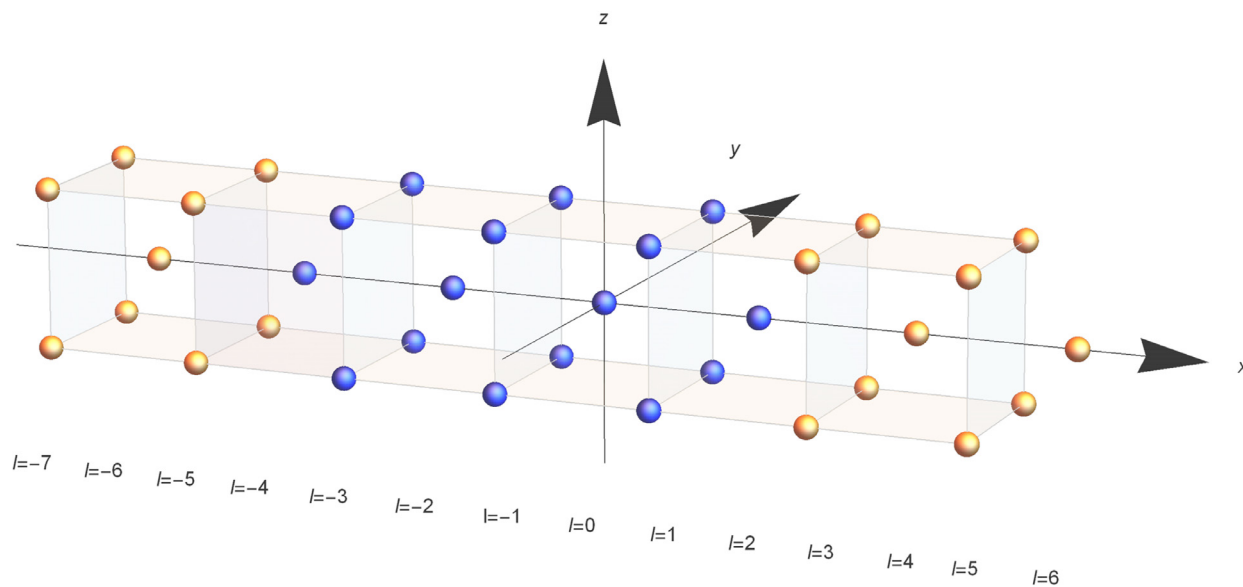
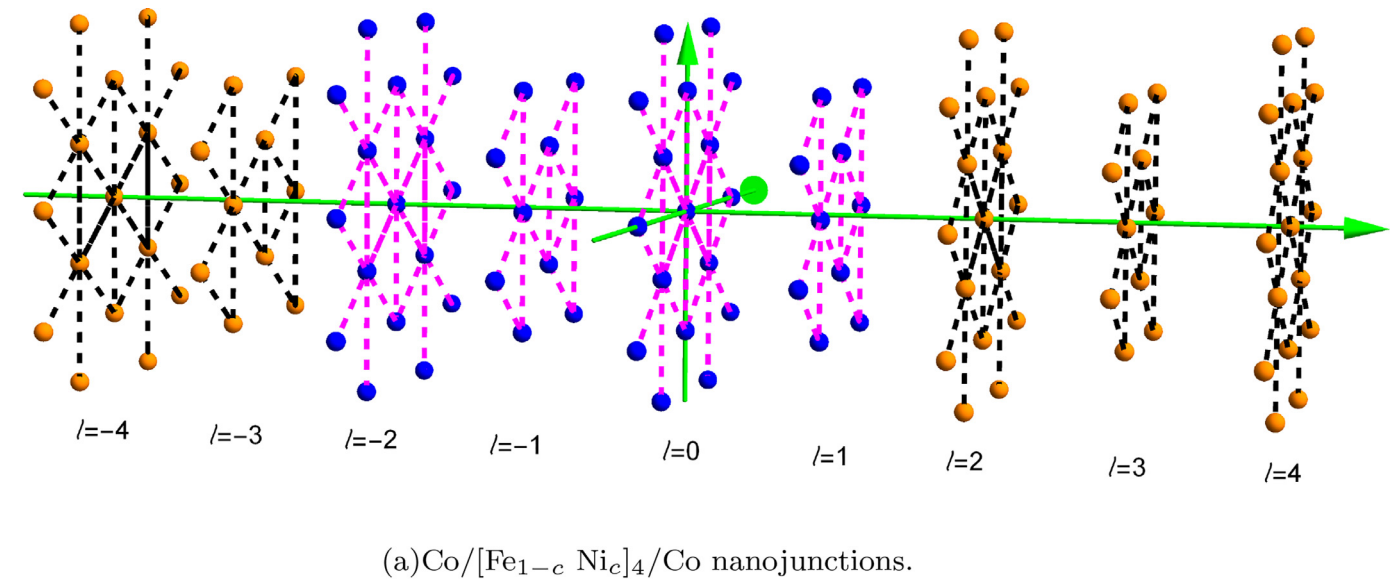


Fig. 1. (Color online) Schematic representations of four and seven layered disordered nanojunctions with Co and Fe leads. Systems with a different number of layers can be sketched in the same way. The orange balls represent Fe/Co leads on both sides of the nanojunctions. The planes of Fe or Ni atoms inside the disordered alloy, whose abundances depend on the concentration c , are represented by blue balls in the nanojunctions with Co and Fe leads respectively. Not all planes involved in the calculation are demonstrated. (For interpretation of the references to color in this figure legend, the reader is referred to the web version of this article.)

allocate an average spin for all the sites in the Fe-Ni alloy nanojunction, namely:

$$S_{av}(c) = (1 - c)S_{Fe} + cS_{Ni}. \quad (1)$$

The spins S_{Fe} and S_{Ni} are quantum numbers characteristic of the individual Fe and Ni atoms, which makes [equation \(1\)](#) a virtual crystal reference for the system. However, the magnetic moments are a function of the electronic density in the neighborhood of the individual atomic sites of Fe and Ni, and these vary depending on the concentrations of the two atomic species.

Despite the fact that the sites can be either iron or nickel, the spin interaction between pairs of nearest neighbours may be treated as an

average quantity, independent of i and j , and as a function of c , so that the configurational average is given by:

$$\langle J_{ij} \rangle = J_{av}(c) = (1 - c)^2 J_{Fe-Fe} + c^2 J_{Ni-Ni} + 2c(1 - c) J_{Fe-Ni}. \quad (2)$$

[Eqs. \(1\) and \(2\)](#) are permitted because experimental measurements using the XMCD, SQUID, and VSM techniques have shown [\[19\]](#), that the weighted sum of the individual magnetic moments of the Ni and Fe sites in a Fe-Ni alloy, agrees very well with the average measured moment per site, for the whole range of alloy concentrations $0 \leq c \leq 1$.

Table 1

Values of the several first neighbour exchange parameters (in meV) using EFT for various values of c pertaining to both bcc and fcc $[\text{Fe}_{1-c}\text{Ni}_c]_n$ structures.

c	$J_{\text{Fe-Fe}}$ (meV)	$J_{\text{Ni-Ni}}$ (meV)	$J_{\text{Fe-Ni}}$ (meV)
0.08,0.13,0.16	18.41	-13.49	12.68
0.65,0.81	-6.02	8.46	20.77

As a second step, assuming that the average exchange parameter of the Fe-Ni alloy coming from EFT is equal to the VCA value given by Eq. (2) allows to derive the configurational average values for the exchange constants found in Table 1. Our new calculations show that both bcc and fcc $[\text{Fe}_{1-c}\text{Ni}_c]_n$ nanojunctions are ferromagnetic contrary to what was previously obtained in [47]. Interestingly, $J_{\text{Ni-Ni}}$ and $J_{\text{Fe-Fe}} < 0$ for bcc and fcc structures respectively meaning that neighbouring Fe sites (Ni sites) are aligned antiparallel in the corresponding alloys. This antiferromagnetic feature has been previously mentioned in the literature where there is some evidence to suggest that $J_{\text{Fe-Fe}}$ is small and negative for the fcc phase [50,51]. In addition, Fe alloys with solutes which stabilize the fcc structure to low temperatures and high Fe concentrations often exhibit antiferromagnetism [52]. [51] quotes a value of -6meV for $J_{\text{Fe-Fe}}$ similar to the one adopted in this work. By the same token, we believe that the antiferromagnetic characteristics of the Ni-Ni interactions in bcc Fe-Ni alloys can be equally interpreted.

2.2. Heisenberg spin dynamics

It is assumed that the structural morphology of the two interfaces between the leads and the nanojunctions are ideally flat. This makes it possible to neglect dipolar interactions at the nanojunctions, as dipolar coupling between two perfectly flat infinite planes vanishes in the absence of interface roughness [53]. The local spin magnetic anisotropy is also smaller than the exchange energy, and can hence be discarded. Moreover due to the slab geometry of the ultrathin nanojunction, the dipolar Zeeman energy is evaluated to be at least two orders of magnitude smaller than the exchange energy [17,54]. These approximations [55], can be applied quite generally to layered ultrathin nanojunctions under the cited conditions.

The spin dynamics of the nanojunction systems is then modeled through a Heisenberg Hamiltonian with the EFT-generated exchange constants, expressed as

$$H = - \sum_{i \neq j} J_{ij} \vec{S}_i \cdot \vec{S}_j. \quad (3)$$

The sum is over all nearest neighbour pairs $\{i, j\}$, where \vec{S}_i and \vec{S}_j denote spin vector variables at sites i and j respectively.

Since the alloy nanojunctions $1 \leq n \leq 7$ are ultrathin with $n \leq 1$ nm, the VCA is an appropriate approximation for the nanojunction when considering SW scattering at wavelengths ≥ 10 nm. The values of J_{ij} can be read from Table 1.

Within the PFMT approach, the nanojunctions are generally divided into three domains [8–10]. The irreducible domain for a four layer nanojunction consists of the planes within the interval $-3 \leq l \leq 2$, l being the plane number as shown in Fig. (1). The convention we adopt is a bit different for nanojunctions with an odd number of layers, where for $n = 7$, the irreducible domain is determined by $-4 \leq l \leq 4$ (Fig. (1)(b)). The matching region separates the alloy from the bulk leads and will be taken to consist of the two planes on the right and on the left of the irreducible domain for bcc nanojunctions and of the three planes on both sides of the irreducible domain for the fcc nanojunctions. The leads (Fe or Co in our case) constitute semi-infinite regions located on either side of the matching regions.

Owing to the presence of the nanojunctions, their 3D spin translation symmetry is broken along the x axis whereas the bcc/fcc symmetries are retained in the yz plane. Hence, it is possible to define the normalized dimensionless phases ϕ_y and ϕ_z , corresponding to wave-vectors k_y and k_z .

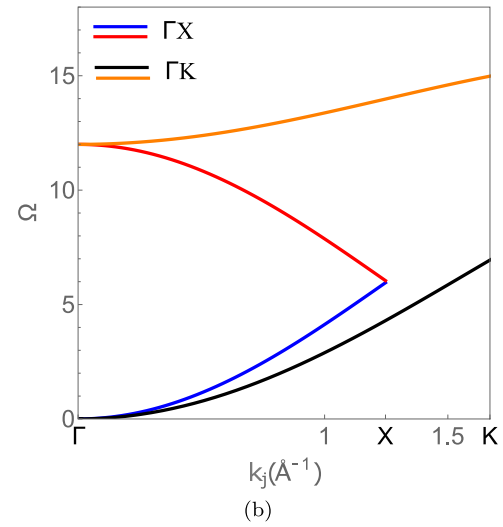
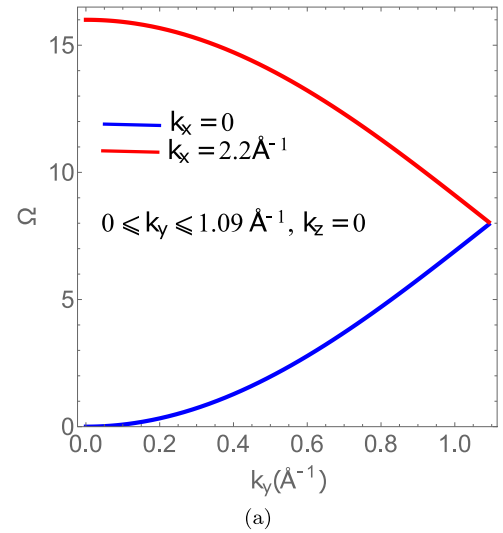


Fig. 2. (Color online) (a) Dispersion curves representing the SW bands generated by the single mode of the Fe leads for $(k_x = 0, k_z = 0)$ and $(k_x = 2.2 \text{ \AA}^{-1}, k_z = 0)$ along $0 \leq k_y \leq 1.09 \text{ \AA}^{-1}$. Propagating waves are identified for $0 \leq \Omega \leq 16$ whereas $\Omega > 16$ correspond to evanescent waves. (b) Dispersion curves for the two characteristic SW modes for hcp Co along two different directions in the Brillouin zone: ΓX corresponding to $k_y = k_z = 0, 0 \leq k_x \leq 1.25 \text{ \AA}^{-1}$ and the ΓK direction defined by $k_x = k_z = 0, 0 \leq k_y \leq 1.67 \text{ \AA}^{-1}$. On the horizontal axis, $j = \{x, y\}$.

For the representative sites on the leads, the spin dynamics is governed by equations of motion for the spin precession amplitudes [8,10,18,56].

2.2.1. bcc Fe

The crystallographic structure of bcc iron results in a single irreducible site in the elementary unit cell, thus yielding a single spin wave mode propagating in the bulk iron lead. The magnon dispersion relation for this SW mode in the Fe semi-infinite leads of an elementary bcc unit cell can be cast in the form [10]:

$$\Omega_{\text{Fe}}(\zeta, \phi_y, \phi_z) = 8 - 4(\zeta + \zeta^{-1}) \cos(\phi_y/2) \cos(\phi_z/2), \quad (4)$$

where $\Omega_{\text{Fe}} = \hbar\omega / (J_{\text{Fe-Fe}} S_{\text{Fe}})$, is a dimensionless energy parameter and $\zeta = e^{i\phi_x/2}$ is a Bloch phase factor. Fig. (2)(a) shows the corresponding calculated acoustical dispersion curves for $(\phi_x = \phi_z = 0)$ and $(\phi_x = 2\pi, \phi_z = 0)$ as a function of k_y where $\phi_y = k_y a_{\text{Fe}}$, a_{Fe} being the lattice parameter for Fe. Propagating waves correspond to $0 < \Omega \leq 16$ and evanescent waves to $\Omega > 16$.

2.2.2. hcp Co

On the other hand, the crystallographic structure of hcp Co results in two inequivalent irreducible sites in the elementary unit cell, giving two spin wave modes that propagate in the bulk Co lead. The system of equations for the spin dynamics for pure semi-infinite Co leads of elementary unit hcp cells may be written in matrix form as [41]:

$$(\Omega_{Co}I - D_B(\zeta, \phi_y, \phi_z))|U_B\rangle = 0. \quad (5)$$

$|U_B\rangle$ is a 2×1 column matrix comprising two elements u_0 and v_0 and represents the vector of the spin precession amplitudes of the two irreducible sites of the 3D unit cell in bulk Co. I is the identity matrix in 2D and $\Omega_{Co} = \hbar\omega/(J_{Co}S_{Co})$ defines the dimensionless energy parameter for Co. J_{Co} and S_{Co} denote the nearest neighbour Co-Co interaction and the spin of bulk Co; they take on the values 15.82 meV and 0.99 respectively obtained via magnetization calculations [16,32,47]. $D_B(\zeta, \phi_y, \phi_z)$ is a spin dynamics matrix of the form:

$$D_B(\zeta, \phi_y, \phi_z) = \begin{pmatrix} d_{11} & d_{12} \\ d_{12}^* & d_{11} \end{pmatrix}, \quad (6)$$

where $d_{11} = -12 + 2 \cos \phi_z + 4 \cos(\phi_z/2) \cos(\sqrt{3}\phi_y/2)$ and $d_{12} = (\zeta + \zeta^{-1})[2e^{i\phi_y/\sqrt{3}} \cos(\phi_z/2) + e^{-i\phi_y/\sqrt{3}}]$. When the magnon dispersion curves for the SW modes are calculated from Eqs. (4) and (5), the $|\zeta| = 1$ region indicates propagating magnon modes, and $|\zeta| < 1$ gives evanescent modes in the leads. Every choice (ϕ_i, ϕ_j) with $i, j = x, y, z$ ($i \neq j$) defines a region in the Brillouin zone (BZ) describing all eigenmode solutions. Whilst evanescent waves do not transport energy, they are nevertheless important for the understanding of the scattering at the nanojunction.

For an hcp Co lattice, there exists two propagating modes $v = 1, 2$ for any value of ϕ_y and ϕ_z under the condition $|\zeta_v| = 1$. The corresponding magnon dispersion curves are shown in Fig. (2)(b) where two directions in the first Brillouin zone are displayed: the ΓX direction along k_x corresponding to $\phi_y = \phi_z = 0$ and the ΓK direction along k_y with $\phi_x = \phi_z = 0$. For the first case, it is evident that the two propagating branches of the magnons occur in the intervals $0 \leq \Omega \leq 6$ and $6 \leq \Omega \leq 12$ giving $|\zeta_1| = |\zeta_2| = 1$, whereas for $\Omega > 6$ and ($\Omega < 6, \Omega > 12$), the waves are evanescent.

3. Sublattice and total magnetizations of the Fe-Ni nanojunctions with Fe/Co Leads

Knowledge of the sublattice and total magnetizations on the different layers of the nanojunctions constitute a preliminary piece of information needed to compute the ballistic transport. Whilst the EFT-VCA approach provides the values of the different exchange parameters, MFT based equations give expressions of sublattice and total magnetizations on the various nanojunction layers. It must be noted that although these features were described in a previous work [47], they will be re-plotted in the current paper using the new adopted values of J .

The spin variables on the l^{th} plane for the nanojunction alloys $[Fe_{1-c}Ni_c]_n$ of n layers, are denoted by $\sigma_\alpha^{(l)}$ and given via Brillouin functions such that:

$$\sigma_\alpha^{(l)} = B_\alpha(S_\alpha, T, H_\alpha) = \frac{2S_\alpha + 1}{2} \coth\left(\frac{2S_\alpha + 1}{2S_\alpha} \frac{H_\alpha^{(l)}}{k_B T}\right) - \frac{1}{2} \coth\left(\frac{1}{2S_\alpha} \frac{H_\alpha^{(l)}}{k_B T}\right). \quad (7)$$

α denotes the atomic element, namely Fe or Ni, S_α the corresponding spin and $H_\alpha^{(l)}$ the molecular field energy for the element α on the l^{th} plane due to interactions with the nearest neighbours. Likewise, the effective magnetic moment per site on the l^{th} plane, $\overline{M}_T^{(l)}$, in units of the Bohr magneton (μ_B) is defined by:

$$\overline{M}_T^{(l)} / \mu_B = (1 - c)g_{Fe}\sigma_{Fe}^{(l)} + cg_{Ni}\sigma_{Ni}^{(l)}, \quad (8)$$

where $g_{Fe}=2.1$ and $g_{Ni}=2.2$ are Landé factors.

Plotting the sublattice magnetization requires to define expressions for each of $H_{Fe}^{(l)}$ and $H_{Ni}^{(l)}$ in terms of $\sigma_{Fe}^{(l)}$ and $\sigma_{Ni}^{(l)}$ which also accommodate the spin exchange constants. Transcendental equations in $\sigma_\alpha^{(kl)}$ are then created and can be solved numerically using *FindRoot* in Mathematica software. Explicit expressions of $\sigma_\alpha^{(l)}$ and $M_T^{(l)}$ for various layers l were thoroughly discussed in [17,18,41,47] and thus will not be repeated here.

3.0.3. Fe/[Fe_{1-c}Ni_c]_n/Fe nanojunctions

Figs. (3)(a), (c) and (e) show the sublattice and total magnetizations on seven layered bcc nanojunctions with Fe leads for $c = 0.16$ as well as the change of the total magnetization on a specific layer as more Ni is injected into the Fe-Ni alloy. We notice that for the bcc case, the sublattice magnetization of Fe remains almost intact on the various layers, except probably for slight variations between the first and fourth layer whereas $\sigma_{Ni}^{(l)}$ shows larger differences on the various layers.

3.0.4. Co/[Fe_{1-c}Ni_c]_n/Co nanojunctions

Additionally, Fig. (3) (b), (d) and (f) represent the sublattice magnetization of Fe and Ni with $c = 0.81$ and the total magnetization as c changes, for four layered fcc nanojunctions with Co leads. These present a more enthralling case where variations in the sublattice magnetizations on different layers are more pronounced for both Fe and Ni. The total magnetization for this type of nanojunctions shows similar characteristics to the bcc type: It is always larger for the layers at the boundaries and becomes smaller for the layers sandwiched inside. The change in the total magnetization for the nanojunctions as c gradually increases is displayed in Fig. (3)(e)–(f): $M_T^{(l)}$ decreases as c increases throughout the whole temperature range; however at room temperature ($k_B T = 25.85 \text{ meV}$), such differences are negligible.

Besides no compensation temperature was observed for any of those systems.

4. The PFMT for magnon ballistic scattering at the nanojunctions

Our interest lies in the energy of the SWs and the total magnon reflection and transmission probabilities across the embedded disordered alloy nanojunctions. The ballistic transport properties are calculated using the PFMT within the framework of the Landauer-Büttiker formalism [42,43]. The equations of motion describing the spin dynamics of magnetic nanostructures are inspected for the representative sites on each layer of the alloy nanojunctions. A single inequivalent site per unit bcc cell will be taken on successive atomic planes for bcc nanojunctions while two inequivalent sites per unit hcp cell will be adopted for the fcc type nanojunctions. The set of atomic sites that will be considered for each value of n embodies the intrinsic symmetry of the system in question.

For the $n = 7$ bcc nanojunctions, we have a set of nine atomic sites in the irreducible domain whose spin precession amplitudes can be represented by: $\{u_{-4}(\text{Fe}), u_{-3}^*(\text{Fe/Ni}), u_{-2}^*(\text{Fe/Ni}), u_{-1}^*(\text{Fe/Ni}), u_0^*(\text{Fe/Ni}), u_1^*(\text{Fe/Ni}), u_2^*(\text{Fe/Ni}), u_3^*(\text{Fe}), u_4(\text{Fe})\}$; the superscript * denotes atomic sites belonging to the alloy and the notation Fe/Ni means that the sites could either be occupied by an Fe or a Ni atom.

The spin precession amplitudes for the irreducible set of atomic sites for a 4-plane fcc nanojunction are represented by $\{v_{-3}(\text{Co}), u_{-2}^*(\text{Fe/Ni}), v_{-1}^*(\text{Fe/Ni}), u_0^*(\text{Fe/Ni}), v_1^*(\text{Fe/Ni}), u_2(\text{Co})\}$, where u and v refer to the two inequivalent sites. Atomic planes belonging to the matching regions contain pure Fe or Co atoms; these are $\{u_{-5}(\text{Fe}), u_{-6}(\text{Fe}), u_5(\text{Fe}), u_6(\text{Fe})\}$ for the $n = 7$ bcc nanojunctions and $\{u_{-6}(\text{Co}), v_{-5}(\text{Co}), u_{-4}(\text{Co}), v_3(\text{Co}), u_4(\text{Co})\}$ and $v_5(\text{Co})\}$ for the $n = 4$ fcc nanojunctions.

Mathematically, the matching regions are expressed through spin precession amplitudes denoted by $w_{i,l,\eta}(v)$, where i labels the atomic sites, v the frequency of the incident SW, and η a fixed number for each case defining the boundary of the irreducible domain. For $n = 4$ nanojunctions, $\eta = -3$ and $\eta = 2$ to the left and right of the alloy respectively, whereas $\eta = -4$ and $\eta = 4$ for $n = 7$ nanojunctions.

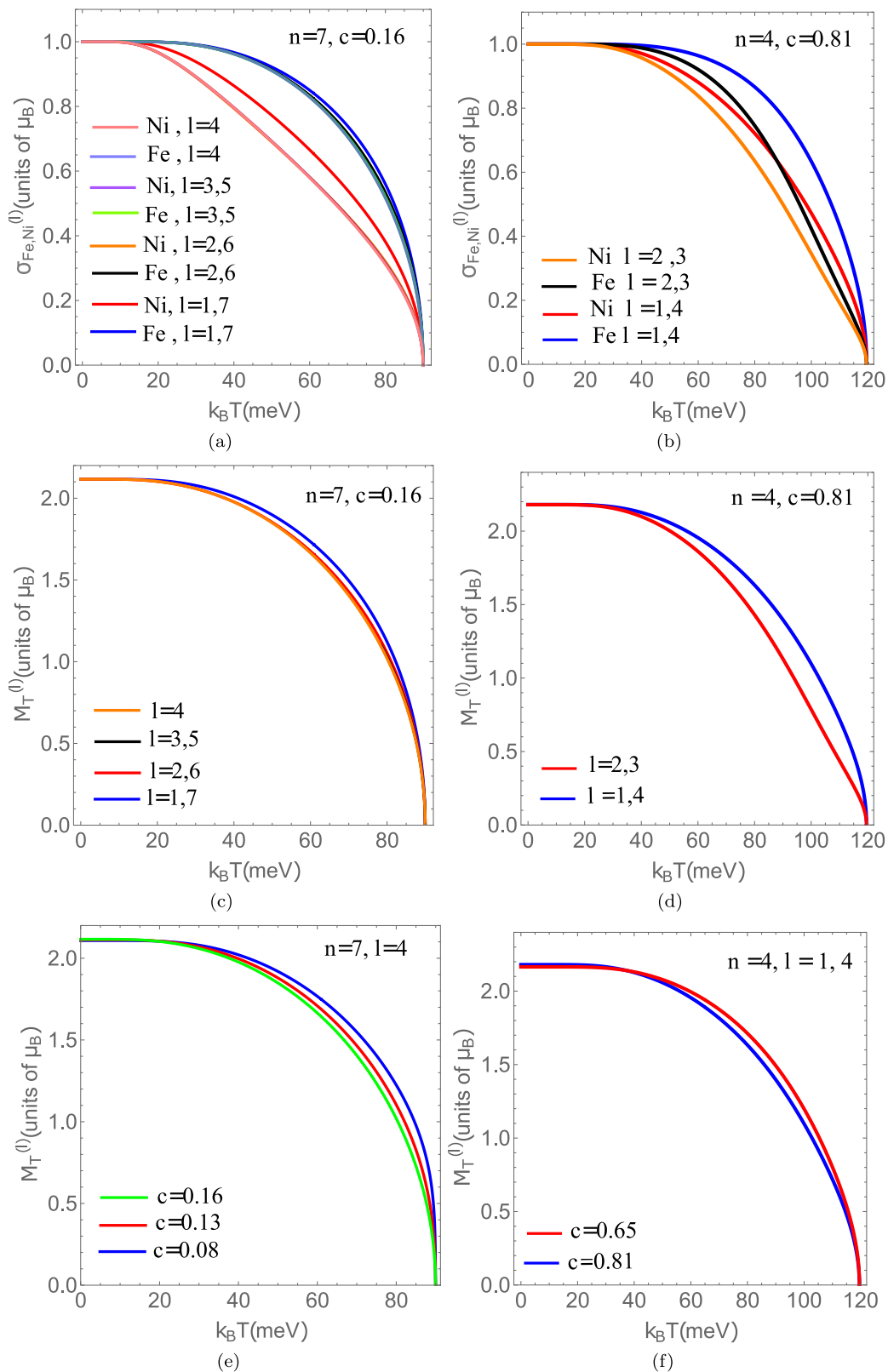


Fig. 3. (Color online)(a)–(d) The sublattice $\sigma_a^{(l)}$ and total magnetization $M_T^{(l)}$ for $n = 7$ bcc ($c = 0.08, 0.13, 0.16$) and $n = 4$ fcc ($c = 0.65, 0.81$) Fe-Ni nanojunctions. (e)–(f) As the concentration of Ni increases, $M_T^{(l)}$ slightly decreases on a specific layer l for both types of nanojunctions. Such changes are negligible at room temperature.

Generally speaking for an incoming magnon mode, along the x axis and related to given wave phase components (ϕ_y, ϕ_z) and energy Ω , the resulting coherent scattering due to the presence of the nanojunction frontier yields reflected and transmitted SW fields in the two semi-infinite iron leads. The full description of the SW scattering can be probed using the PFMT method, where it is crucial to know the evanescent as well as the propagating eigenmodes of the leads to understand the sophisticated mechanism engaged in the scattering processes.

For a given incident SW mode ν from the Fe/Co leads on the left hand side onto the embedded nanojunction, the spin precession amplitudes $w_{i,l,\eta}(\nu)$ for the inequivalent atomic bcc/fcc sites (planes) on the left side, may be written as the superposition of contributions coming from the incident SW field and the backscattered fields at the same frequency and wave-vector components, at that particular plane l , ($l < \eta, \eta < 0$):

$$w_{i,l,\eta}(\nu) = e_i(\nu)\zeta_\nu^{(l-\eta)} + \sum_{\nu'} r_{\nu\nu'} e_i(\nu')\zeta_{\nu'}^{(\eta-l)}. \quad (9)$$

Likewise, for the inequivalent atomic sites on the right side, into which the incident SW mode ν is transmitted, the emerging spin precession amplitudes may be expressed by another appropriate superposition of the contributions from the forward scattered fields at the same frequency and wave-vector components at that specific atomic plane l ($l > \eta, \eta > 0$).

$$w_{i,l,\eta}(\nu) = \sum_{\nu'} t_{\nu\nu'} e_i(\nu')\zeta_{\nu'}^{(l-\eta)}. \quad (10)$$

The elements $r_{\nu\nu'}$ and $t_{\nu\nu'}$ in the above equations, denote the reflection and transmission coefficients respectively describing the scattering from the incident SW mode ν into the ensemble of the available eigenmodes ν' , and are in conformity with the Landauer-Büttiker formalism. $e_i(\nu)$ is (are) the eigenvector(s) on the Fe (Co) lead at the given incident frequency and wave-vector components obtained by solving the relations leading to Eqs. (4) and (5) for bulk Fe (Co).

In order to solve for the reflection and transmission inside the nanojunction, it is instructive to construct a Hilbert space with state vectors, that we call $|U'\rangle$, made from the basis vectors $|r\rangle$, $|t\rangle$ and $|U_{nano}\rangle$, where $\{|r\rangle, |t\rangle\}$ are the vectors corresponding to the ballistic reflection and transmission processes and are made up of the elements $r_{\nu\nu'}$ and $t_{\nu\nu'}$. $|U_{nano}\rangle$ contains the spin precession amplitudes for the irreducible set of atomic sites for the nanojunction. To be more clear, for the bcc Fe/[Fe_{1-c}Ni_c]₇/Fe nanojunction,

$$|U'\rangle = \{u_{-4}(Fe), u_4(Fe), u_{-3}^*(Fe/Ni), u_3^*(Fe/Ni), u_{-2}^*(Fe/Ni), u_2^*(Fe/Ni), u_{-1}^*(Fe/Ni), u_1^*(Fe/Ni), u_0^*(Fe/Ni), |r\rangle, |t\rangle\},$$

which has thirteen components whereas for the fcc Co/[Fe_{1-c}Ni_c]₄/Co nanojunction, it comprises ten components:

$$|U'\rangle = \{v_{-3}(Co), u_{-2}^*(Fe/Ni), v_{-1}^*(Fe/Ni), u_0^*(Fe/Ni), v_1^*(Fe/Ni), u_2(Co), |r\rangle, |t\rangle\}.$$

Generally, to obtain the magnonic dispersion curves, one has to solve a matrix equation involving $|U'\rangle$:

$$D_s^{(7)}(\gamma_j, \{\zeta_\nu\}, \phi_y, \phi_z)_{[11 \times 11]} |U'\rangle_{[11 \times 1]} = -|IH_\nu\rangle_{[11 \times 1]}, \quad (11)$$

for a 7 layered bcc nanojunction with Fe leads. On the other hand, for a 4-layer fcc nanojunction with Co leads, the matrix equation has a different dimension and looks like:

$$D_s^{(4)}(\gamma_j, \{\zeta_\nu\}, \phi_y, \phi_z)_{[10 \times 10]} |U'\rangle_{[10 \times 1]} = -|IH_\nu\rangle_{[10 \times 1]}, \quad (12)$$

where in both cases $D_s^{(4,7)}$ are inhomogeneous square matrices of dimensions 10×10 and 11×11 . The column vector $|IH_\nu\rangle$, mapped appropriately on to the basis vectors in the Hilbert space, collects the inhomogeneous terms describing the incident spin wave. In more details,

for nanojunctions with Fe leads and $n = 7$, the matched spin matrix $D_s^{(7)}$ is the product of two rectangular matrices and can be split into:

$$D_s^{(7)}(\gamma_j, \{\zeta_\nu\}, \phi_y, \phi_z)_{[11 \times 11]} = D_{d,[11 \times 13]}^{(7)} D_{R,[13 \times 11]}^{(7)}, \quad (13)$$

$D_R^{(7)}$ is made of block matrices and assumes the form:

$$D_{R,[13 \times 11]}^{(7)} = \begin{pmatrix} I & J \\ K & L \end{pmatrix},$$

where $I = I_{[9 \times 9]}$ is the Identity matrix, $J = J_{[9 \times 2]}$ and $K = K_{[4 \times 9]}$ are zero matrices and L is a 2×1 column matrix whose first element is $\begin{pmatrix} \zeta & 0 \\ 0 & \zeta \end{pmatrix}$, and second element is $\begin{pmatrix} \zeta^2 & 0 \\ 0 & \zeta^2 \end{pmatrix}$.

Variouly, for an $n = 4$ nanojunction with Co leads, $D_s^{(4)}$ can be written as a product:

$$D_s^{(4)}(\gamma_j, \{\zeta_\nu\}, \phi_y, \phi_z)_{[10 \times 10]} = D_{d,[10 \times 12]}^{(4)} D_{R,[12 \times 10]}^{(4)}, \quad (14)$$

where again,

$$D_{R,[12 \times 10]}^{(4)} = \begin{pmatrix} I & J \\ K & L \end{pmatrix}.$$

In this case, I is a 6×6 matrix, J a 6×4 matrix, K a 6×6 matrix and L a 6×4 matrix given by:

$$L = \begin{pmatrix} 0 & 0 & \zeta_1 e_1(1) & \zeta_2 e_2(2) \\ \zeta_1 e_2(1) & \zeta_2 e_2(2) & 0 & 0 \\ 0 & 0 & \zeta_1^2 e_1(1) & \zeta_2^2 e_1(2) \\ \zeta_1^2 e_1(1) & \zeta_2^2 e_1(2) & 0 & 0 \\ 0 & 0 & \zeta_1^3 e_2(1) & \zeta_2^3 e_2(2) \\ \zeta_1^3 e_2(1) & \zeta_2^3 e_2(2) & 0 & 0 \end{pmatrix}.$$

$e_i(\nu)$ ($i = 1, 2$) are the eigenvectors of the dynamic spin matrix on the semi-infinite cobalt leads. Setting the determinants of $D_s^{(4,7)}$ equal to zero allows to determine the propagating and localized spin states of the system as well as extract $r_{\nu\nu'}$ and $t_{\nu\nu'}$ necessary to calculate the reflectance and transmittance for a spin wave incident on the nanojunction.

The reflection $R_{\nu\nu'}$ and transmission $T_{\nu\nu'}$ cross sections (probabilities), giving a complete description of the scattering process for the embedded nanojunction, are then written as:

$$R_{\nu\nu'}(\phi_y, \phi_z, \Omega) = (v_{g\nu'} / v_{g\nu}) |r_{\nu\nu'}|^2 \quad (15)$$

$$T_{\nu\nu'}(\phi_y, \phi_z, \Omega) = (v_{g\nu'} / v_{g\nu}) |t_{\nu\nu'}|^2, \quad (16)$$

where $v_{g\nu} = d\Omega/d\phi_x$ is the magnon group velocity corresponding to eigenmode ν and is equal to zero for evanescent modes. R and T must be normalized with respect to $v_{g\nu}$ to ensure the unitarity of the scattering matrix.

Practically, the total reflection R_ν and total transmission T_ν cross sections, for a certain propagating eigenmode ν are retrieved by summing over all contributions of the scattered eigenmodes ν' , and written as:

$$R_\nu(\phi_y, \phi_z, \Omega) = \sum_{\nu'} R_{\nu\nu'}(\phi_y, \phi_z, \Omega) \quad (17)$$

$$T_\nu(\phi_y, \phi_z, \Omega) = \sum_{\nu'} T_{\nu\nu'}(\phi_y, \phi_z, \Omega) \quad (18)$$

Total reflection and transmission (the so called conductance) parameters can also be prescribed summing over all input and output propagating SW modes:

$$R(\phi_y, \phi_z, \Omega) = \sum_{\nu, \nu'} R_{\nu\nu'}(\phi_y, \phi_z, \Omega) \quad (19)$$

$$T(\phi_y, \phi_z, \Omega) = \sum_{\nu, \nu'} T_{\nu\nu'}(\phi_y, \phi_z, \Omega). \quad (20)$$

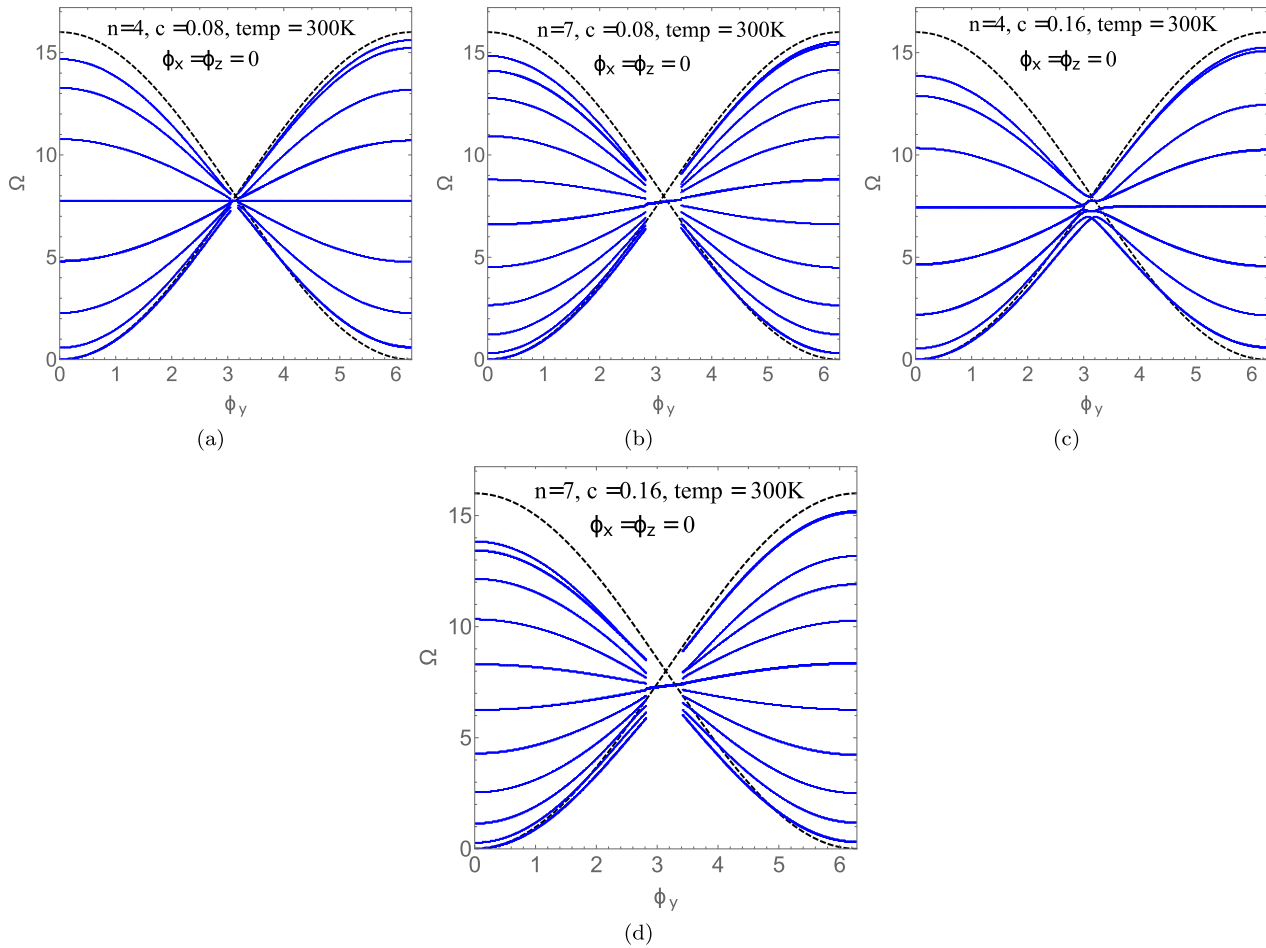


Fig. 4. (Color online) (a)–(d) The blue curves are the magnon dispersion curves for $n = 4, 7$ bcc nanojunctions with Fe leads at room temperature for $c = 0.08, 0.16$ plotted along the path ($\phi_x = \phi_z = 0, 0 \leq \phi_y \leq 2\pi$) showing both the “in resonance” and localized SW modes. The dashed dispersion curves outline the SW bands generated by the single mode of the Fe leads.

Without loss of generality, the conditions $R_\nu + T_\nu = 1$ for each mode ν and $R + T = 1$ must always be satisfied. The mathematical tools detailed above are the same as those adopted in other nanojunction systems with Fe [18] and Co leads [41].

The conductance, corresponding to a physically measurable quantity, as well as the thermal transport across the embedded nanojunction [8,54] can be also deduced from our results which could be otherwise calculated by means of non equilibrium Green functions formalism, or DFT using maximally localized Wannier functions (MLWF) [57,58]. However PFMT is computationally more efficient, easier to implement and allows to solve different scattering problems [59] in a straightforward manner.

5. Results and discussion

5.0.5. Magnonic dispersion branches

The excitations in the form of spin resonance modes are numerically computed by solving the eigenvalue problem for the inhomogeneous PFMT spin dynamics matrix for both types of nanojunctions whose mathematical details are found in [18,41]. The dispersion curves for these excitations are given as continuous plots in Fig. (4)(a)–(d) related to bcc nanojunctions whereas Fig. (5)(a)–(e) are those corresponding to fcc nanojunctions with Co leads. Calculations are shown for both $n = 4$ and $n = 7$ bcc and fcc nanojunctions to examine the effect of increasing the number of layers for a single type of nanojunctions. The dashed curves are dispersion spectra for the pure Fe/Co leads along the

irreducible BZ paths shown in Fig. (2). It is essential to state that our method allows the computation of the dispersion curves along any arbitrary direction, as is shown in Fig. (5)(e) where the branches are taken to belong to a different path ($\phi_x = \phi_y = 0, 0 \leq \phi_z \leq 2.3$), for fcc nanojunctions.

Firstly, we realize that the number of dispersion curves increases with increasing thickness for both nanojunctions. Secondly there are two types of propagating spin states in both systems. We shall refer to them as the “in resonance” and localized states. The former represents modes which propagate in the plane of the nanojunctions whose dispersion lies inside the projected Fe/Co bulk magnon modes whereas the latter also propagate inside the plane of the nanojunction with their amplitudes in the direction normal to the plane of the nanojunction; however they appear as branches crossing the projected Fe/Co bulk magnon modes. While the usual form of the localized magnon modes observed in other similar systems cut across the lead magnon bands growing in number as more layers are stacked [18,41], the localized modes in the Fe-Ni systems present themselves as ordinary branches of magnons.

At normal incidence, the localized modes are always attributed to the lowest dispersion branches; for instance in the case of a seven layered fcc nanojunction with $c = 0.81$, they belong to the first four branches with $\Omega \in [\sim 0 \text{ to } 7.4], [\sim 0.25 \text{ to } 7.93], [\sim 0.75 \text{ to } 8.73]$ and $[\sim 1.68 \text{ to } 9.45]$ respectively. For the path corresponding to ($\phi_x = \phi_y = 0, 0 \leq \phi_z \leq 2.3$), such localized modes occur in a higher range of Ω namely within the $[\sim 12.26 \text{ to } 15.43]$ interval for the $n = 7, c = 0.65$ case.

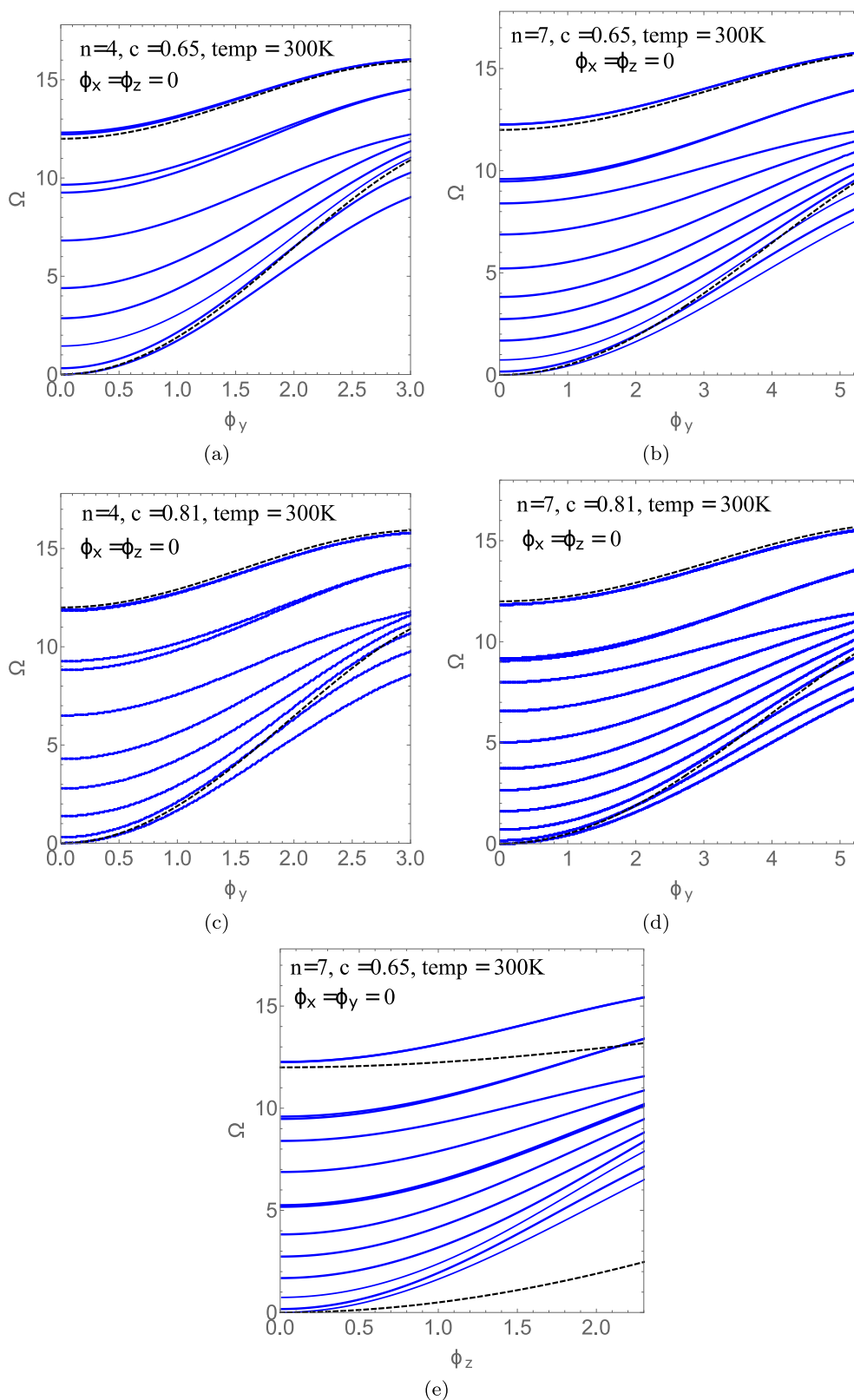


Fig. 5. (Color online) Same as Fig. 4) but for fcc nanojunctions with $c = 0.65, 0.81$ plotted along the y-direction ($\phi_x = \phi_z = 0, \phi_y$) and along ($\phi_x = \phi_y = 0, 0 \leq \phi_z \leq 2.3$) representing both the “in resonance” and localized SW modes. The dashed dispersion curves are SW bands generated by the two modes of the Co leads.

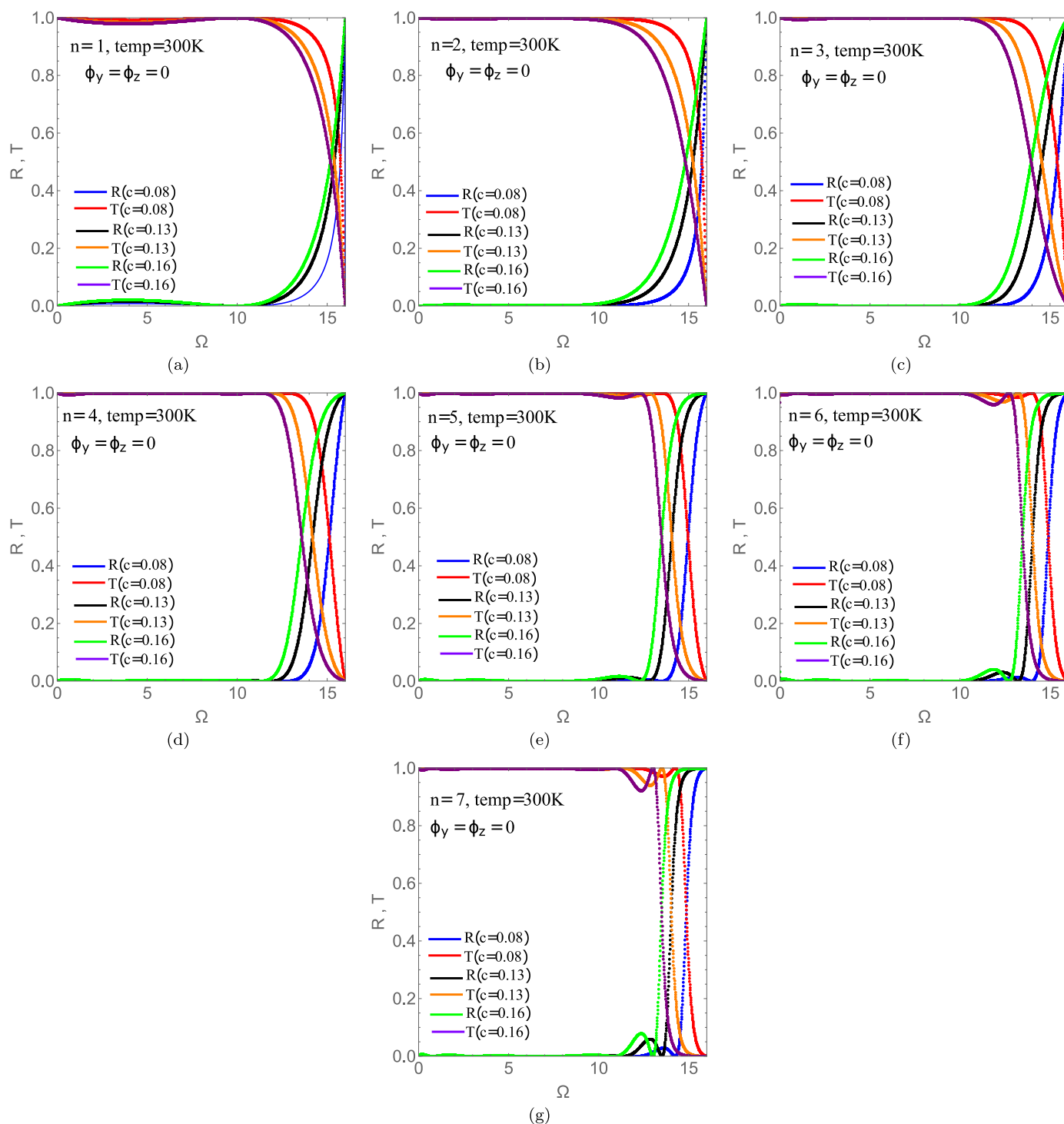


Fig. 6. (Color online) (a)–(g) The reflection R and transmission T cross sections for the ballistic transport of SWs within the bcc nanojunctions at normal incidence ($\phi_y = \phi_z = 0$) for $c = 0.08, 0.13,$ and 0.16 . Transmission maxima start to emerge for $n \geq 5$ in the high frequency regime.

5.0.6. Reflectance (R) and transmittance (T)

Another benefit of solving the PFMT based equations is the ability to investigate the scattering effects in the nanojunctions by gathering information about the R and T parameters for a given incident SW mode ν . They are a consequence of the interactions of the incident modes with the spin resonances on the nanojunction. These were determined along a few paths in the BZ including the normal incidence case ($\phi_y = \phi_z = 0$) for both kinds of nanojunctions. On the other hand, for the fcc nanojunctions, the R_1 and T_1 curves refer to the lowest frequency incident mode (lower frequency mode) coming from the bulk Co leads.

Tables 2 and 3 display the maximum transmittance values associated with the ballistic scattering at the bcc and fcc nanojunctions, presented in Figs. (6) and (7). These correspond to a constructive interference between the various transmitted magnons. To numerically extract the maximum positions, the package *Select* in Mathematica software was used such that only the spectral peaks satisfying the precision condition, $0.9996 \leq T \leq 1$ are reported.

At normal incidence ($\phi_y = \phi_z = 0$), the number of maxima, which start to emerge for $n \geq 2$, increases as the fcc nanojunctions gain more layers. For a fixed number of layers, they tend to shift to a lower

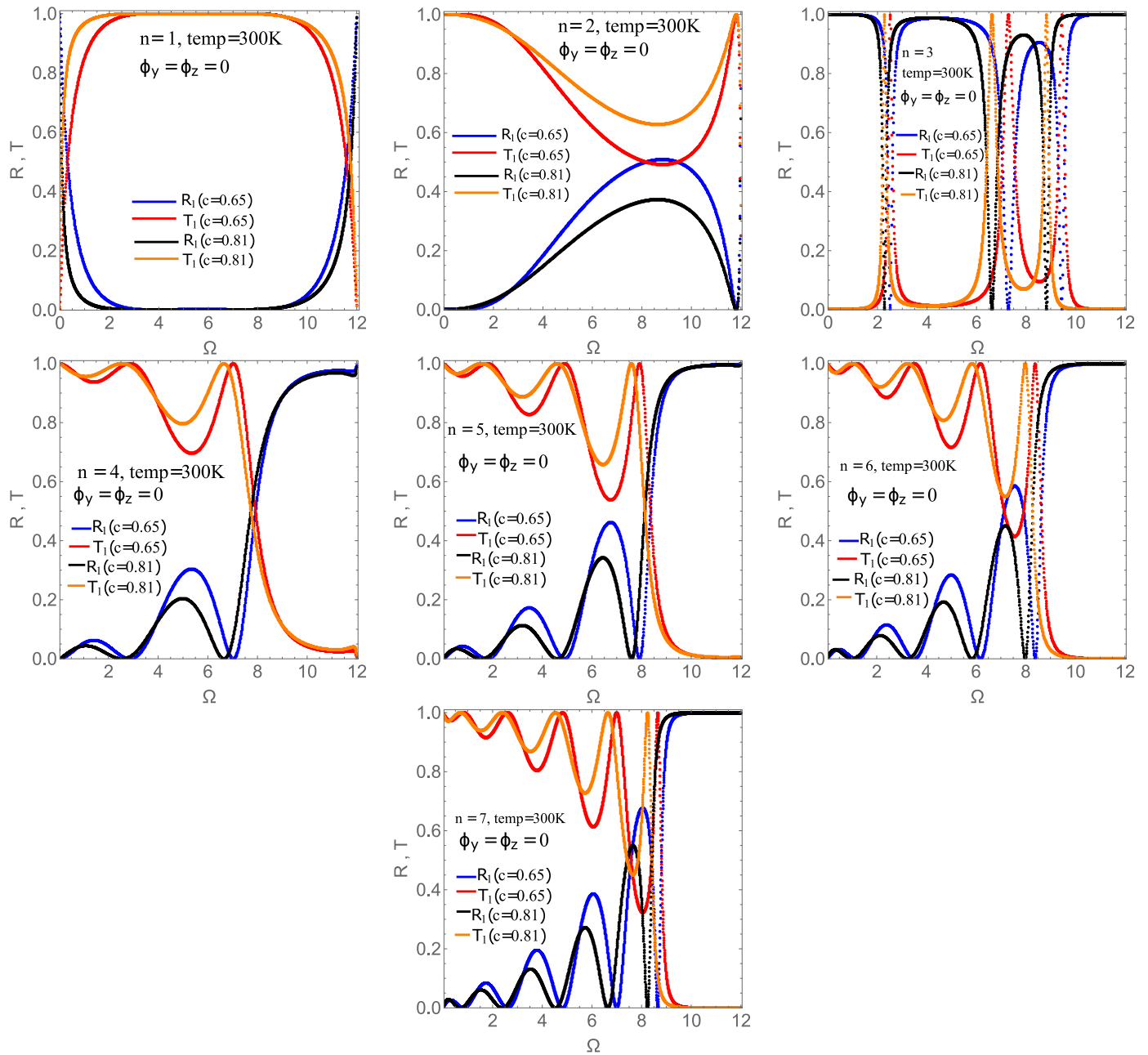


Fig. 7. (Color online) The reflection R_1 and transmission T_1 cross sections for the ballistic transport of the SWs in fcc nanojunctions for mode 1 (lower frequency mode) at normal incidence ($\phi_y = \phi_z = 0$) with $c = 0.65, 0.81$. R_2 and T_2 pertaining to the higher frequency mode can be similarly plotted.

Table 2

Values of the normalized energies Ω at which $0.9996 \leq T(\Omega, \phi_y, \phi_z) \leq 1$ for different bcc nanojunctions of thickness $5 \leq n \leq 7$, concentrations $c = 0.08, 0.13, 0.16$, computed at normal incident angles ($\phi_y = \phi_z = 0$) and room temperature 300K.

Concentration c	Thickness n	Peak positions Ω
0.08	5	13.48
	6	13.96
	7	14.25
0.13	5	12.79
	6	13.22
	7	13.51
0.16	5	12.26
	6	12.72
	7	13.01

Table 3

Same as Table 2 but for different fcc nanojunctions with concentrations $c = 0.65$ and 0.81 and $2 \leq n \leq 7$, computed at room temperature 300K.

Concentration c	Thickness n	Peak positions Ω
0.65	2	11.82
	3	2.51, 7.29, 9.45
	4	2.85, 7.02
	5	1.77, 4.89, 7.91
	6	1.17, 3.51, 6.17, 8.38
	7	0.81, 2.59, 4.81, 6.99, 8.65
	0.81	2
3		2.28, 6.62, 8.82
4		2.54, 6.64
5		1.55, 4.60, 7.59
6		1.00, 3.24, 5.84, 7.98
7		0.70, 2.38, 4.52, 6.64, 8.24

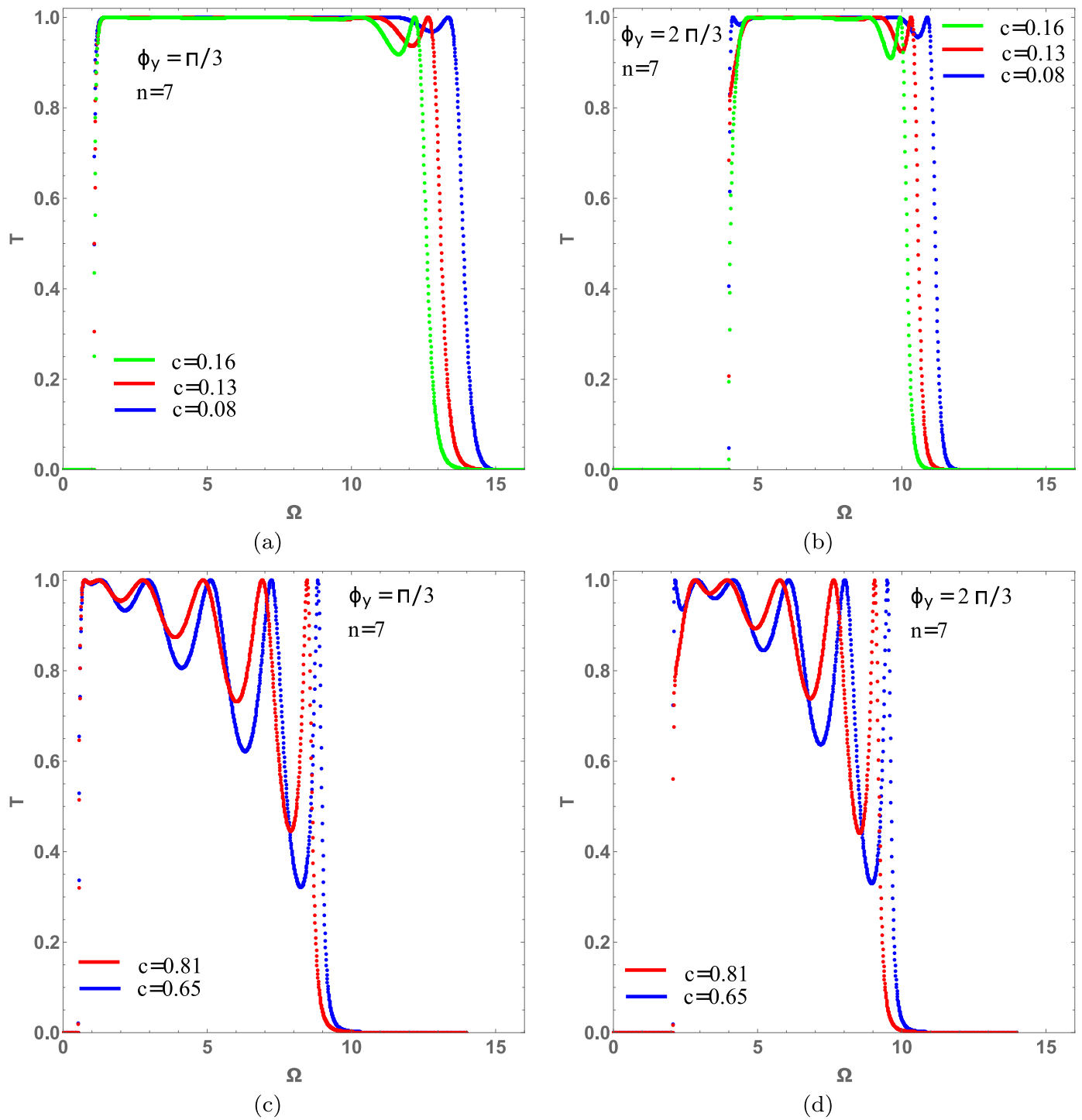


Fig. 8. (Color online) (a)-(b)The transmittance $T(\Omega)$ for $n = 7$ bcc nanojunctions corresponding to $c = 0.08, 0.13$ and 0.16 along two specific directions ($\phi_y = \pi/3, 2\pi/3$ with $\phi_z=0$) in the BZ emphasizing both the effect of sending the SW along directions other than the normal direction and the response upon increasing the Ni concentration c . (c)-(d) Same as (a)-(b) but for fcc nanojunctions with $c = 0.65$, and 0.81 .

frequency value as c increases. This is due to the magnon scattering which is somehow similar to a Rayleigh scattering of waves by particles [44,45]; to get more transmission as the size of the particle increases, one should increase the wavelength and thus lower the frequency. For bcc nanojunctions, the maxima, only starting to occur for $n \geq 5$ in the high frequency regime, remain at the same positions. On an experimental (practical) level, this variety may have implications on the properties of each of the n -layered nanojunctions. It should be reminded that the estimated total reflection and transmission cross sections satisfy the uni-

arity condition, that is $R_\nu + T_\nu = 1$ for each SW mode ν incident from the Fe/Co leads.

5.0.7. Variation of the path in the BZ

The variation of the peak positions for which the transmission T is maximum along different paths of the BZ inside the nanojunctions, as well as the effect of changing the concentration of Ni on such positions are both worth investigating. This is advantageous for the study of the change in transmittance along several directions in the reciprocal space,

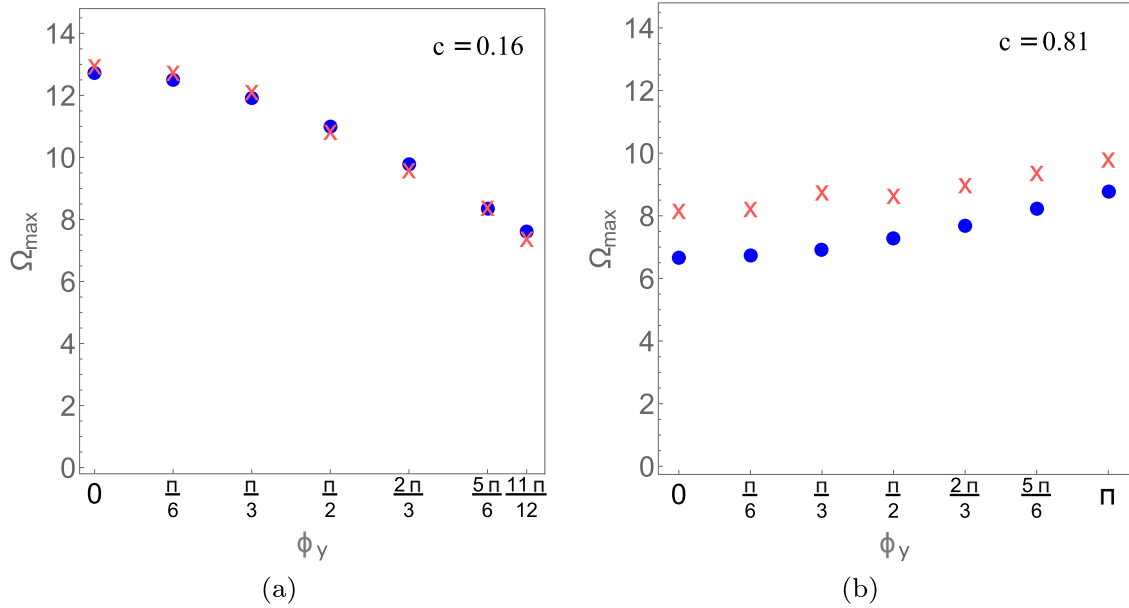


Fig. 9. (Color online) (a) The highest mode, Ω_{max} , at which the transmittance T is maximum for $n = 6$ (\bullet) and $n = 7$ (\times) layered bcc nanojunctions with $c = 0.16$ along a few directions in the BZ. (b) Same as (a) but for fcc nanojunctions with $c = 0.81$, $n = 4$ (\bullet) and $n = 7$ (\times).

in particular to detect at what frequencies maximum transmittance takes place. This is considered to be extremely helpful while fabricating such nanojunctions for industrial applications especially in the areas of spin wave magnonics and spin based nanoelectronics, assuming that we can technologically tune the wavelength at several energies and incidence directions.

Fig. (8) involves $n = 7$ bcc and fcc nanojunctions along two different BZ directions, namely $\phi_y = \pi/3$ and $\phi_y = 2\pi/3$ with $\phi_z = 0$. For a fixed direction in the BZ considered in this work, the maxima tend to shift to lower values of Ω as we increase c , a behavior common to both types of nanojunctions. Yet, for a given c , the maxima along the $\phi_y = 2\pi/3$ direction appear to be shifted to lower values compared to those corresponding to $\phi_y = \pi/3$ in bcc nanojunctions. The contrary happens for fcc nanojunctions where the maxima seem to move to higher frequency values as we go from $\phi_y = \pi/3$ to $\phi_y = 2\pi/3$.

This trend continues to be observed when we further explore the BZ or increase the number of layers as is illustrated in Fig. (9) representing the variation of Ω_{max} , corresponding to a maximum transmittance ($T_{max} = 1$), as a function of different directions in the BZ at two different thicknesses. This was investigated for $n = 6, 7$ and $n = 4, 7$ for bcc and fcc types respectively. The reason behind choosing $n = 6$ for the bcc case is that spectral peaks only start to manifest for $n \geq 5$. As we span the BZ, Ω_{max} for 16% Ni bcc nanojunctions gradually decrease in number, thus moving to the low frequency regime. On the contrary, those for fcc nanojunctions with $c = 0.81$ shift to the high frequency regime as we move away from the normal incidence direction.

5.0.8. The effect of temperature

The transmission behavior as temperature is increased is the subject of Fig. (10). Figs. (10)(a)–(c) give the group velocities of the magnon modes of bulk Fe and Co over their propagating intervals at temperatures higher than the ambient temperature. Raising the temperature of multilayered bcc nanojunctions causes new maxima to emerge and become more defined at a temperature of 881.67K ($k_B T = 76\text{meV}$), as opposed to the single peaks at ambient temperatures. For $c = 0.16$, $n = 7$, seven maximum peaks arise at positions 0.98, 2.55, 4.18, 5.89, 7.72, 9.68 and 11.38. On the other hand, fcc nanojunctions will have all their five localized maxima, with no new peaks appearing, switch to lower values as $k_B T$ inflates: The maxima located at positions 0.7, 2.38, 4.53, 6.64 and 8.24 at ambient temperature move to 0.52, 2.00, 4.16, 6.12,

and 7.69 at a temperature of 580.05K ($k_B T = 50\text{meV}$) and further decrease to 0.41, 1.64, 3.66, 5.37 and 6.90 at 754.06 K ($k_B T = 65\text{meV}$). We expect that at higher temperatures, close to the Curie temperature of Co, the localized maxima squeeze more towards lower frequencies, hence reducing the transmittance range for the nanojunctions. This makes sense since any gain in temperature causes the sublattice magnetizations of Fe and Ni inside the nanojunctions to decrease, destroying the nanojunctions' ability to transmit at wide frequency ranges. Despite this fact, we can still benefit from the nanojunctions (especially bcc ones) at temperatures reasonably larger than 300K if the goal is to target specific transmission frequencies.

6. Summary and conclusion

In the present work, a full analysis of the scattering effects and ballistic transport properties for SW incident from Fe/Co leads across Fe-Ni alloy nanojunctions $\text{Fe}_{1-c}\text{Ni}_c$ is established for $1 \leq n \leq 7$ and various concentrations c showing a diversity in the results obtained. For our purposes, $c \leq 0.25$ will define a bcc nanojunction and $c \geq 0.60$ refer to fcc nanojunctions. According to the model we adopted in this publication, all nanojunctions are ferromagnetic with spins $S_{Fe} = S_{Ni} = 1$. The spin exchange parameters were calculated within an Ising-EFT model making use of the VCA and reliable experimental T_c values.

PFMT, a method identical to the non equilibrium Green functions but considered more transparent and less computationally demanding, is exploited to examine the scattering effects in compliance with the Landauer-Büttiker formalism. This is a robust technique used mainly when one or more directions break the translational symmetry in the systems and is beneficial to treat other types of waves such as phonons and electrons. In our current paper, the broken symmetry of the nanojunctions is only along the x-axis, normal to their plane, giving rise to several spin wave excitations on that axis and in the vicinity of the nanojunctions. These excitations that were numerically computed are spin wave resonance modes forming dispersion curves.

The reflectance and transmittance dictating the ballistic SW transport at the nanojunction for the different multilayered nanojunctions between the two semi infinite Fe/Co leads were examined by sending SW along various incidence directions incorporating the trivial normal incidence case ($\phi_y = \phi_z = 0$). The effects of adding more layers and enriching the nanojunctions with Ni were also considered. It was remarked

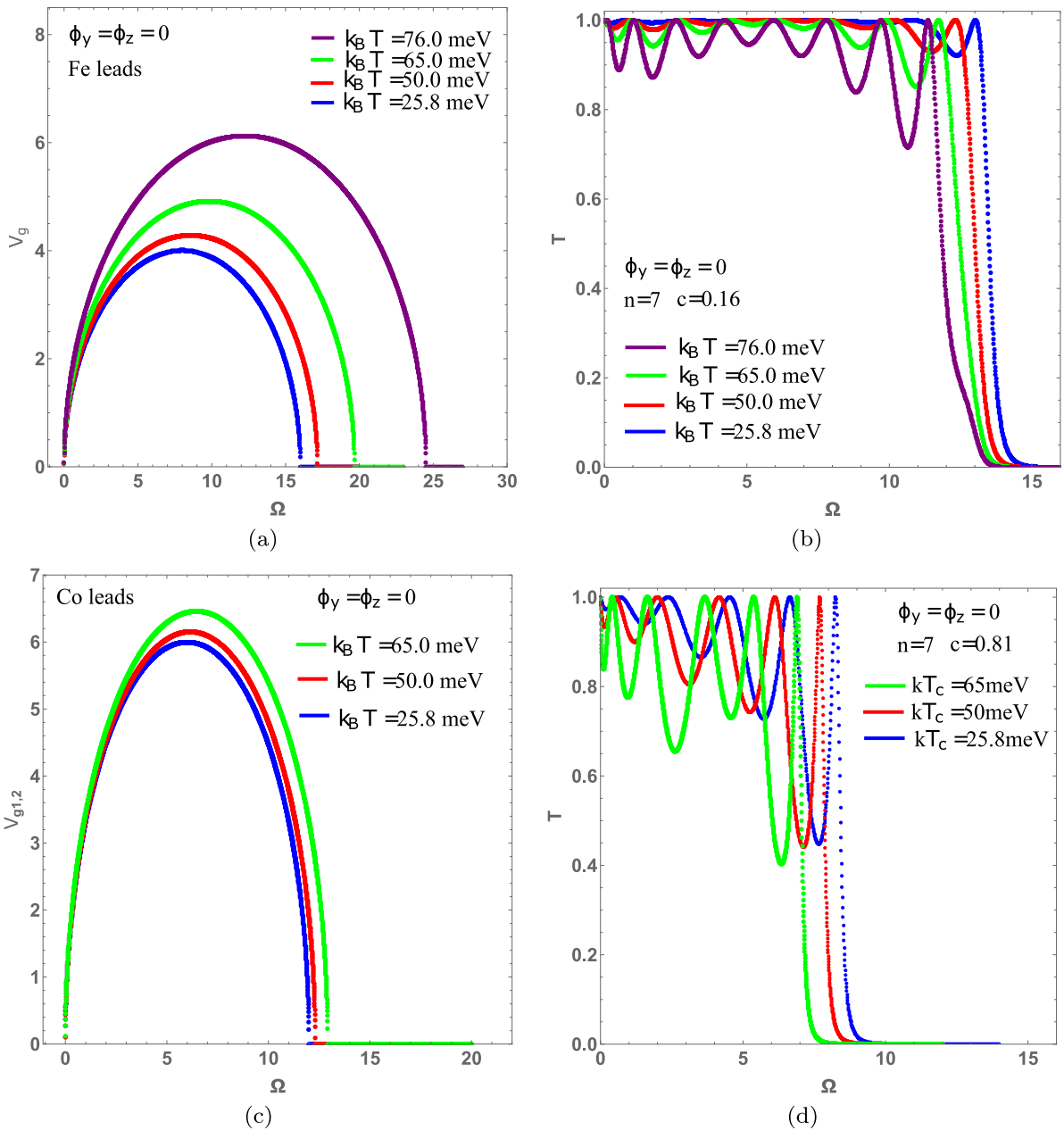


Fig. 10. (Color online) (a)–(c) Group velocities of the magnon modes at normal incidence for the Fe and Co leads respectively at the chosen temperatures. (b) Transmission along the normal incidence direction at $k_B T = 50, 65$ and 76 meV compared to the ambient temperature $k_B T = 25.85$ meV for $n = 7$ bcc nanojunctions with Fe leads. New transmission maxima appear and become well defined as the temperature approaches $k_B T_c = 76$ meV. (d) Same as in (b) but for fcc nanojunctions with Co leads at $k_B T = 50, 65$ meV also set in comparison with that at ambient temperature.

that both systems show two types of modes in their dispersion curves: “in resonance” and “localized” where the latter type also propagates perpendicularly to the plane of the nanojunctions, and appear as ordinary branches of the bulk magnon modes; this is a new feature not depicted in the magnetic nanojunctions previously considered where the nanojunctions’ magnonic branches clearly cut through the bulk modes. Besides, the fcc nanojunctions show transmission maxima peaks at specific frequencies which both increase in number and shift towards low energy modes as c increases whereas for the bcc nanojunctions, the maxima only occur at high energy modes.

Other properties of the nanojunctions investigated in this work could also be taken advantage of; for example along a particular incidence direction of the bcc nanojunctions, the highest modes at maximum transmission tend to shift to a lower frequency region as we move from one

direction to another in the BZ. On the contrary, they shift to higher values in fcc nanojunctions.

Raising the temperature above 300K at normal incidence has a remarkable effect in multilayered bcc nanojunctions: more maxima start to emerge throughout the whole frequency regime, becoming more defined when the temperature reaches ~ 882 K. For fcc nanojunctions, no new maxima arise but those already existing shift to lower frequencies.

Ultimately, it is important to state that our results are accurate in the range between nanometric SW wavelengths, greater than the nanojunction width, and macroscopic wavelengths. The relevance in experimental magnonics research are spectral transmission values for low frequency SW which in fact correspond to longer submicroscopic wavelengths. However, for short SW wavelengths, the VCA-PFMT model fails to exactly describe the ballistic transmission properties of

the nanojunction. Within this wavelength range, a different approach such as the Dyson formalism and possibly a non local CPA technique [60] should be applied.

Declaration of interests

The authors Elie A. Moujaes, A. Khater, M. Abou Ghantous and V. Ashokan certify that they have no affiliations with or involvement in any organization or entity with any financial interest or non-financial interest (such as personal or professional relationships) in the subject matter or materials discussed in this article.

References

- [1] D. Weller, A. Moser, Thermal effect limits in ultrahigh-density magnetic recording, *IEEE Trans. Magn.* 35 (1999) 4423.
- [2] J. Barnas, I. Weymann, Spin effects in single-electron tunnelling, *J. Phys.: Condens. Matter* 20 (2008) 423202.
- [3] A.K. Santra, D.W. Goodman, Oxide-supported metal clusters: models for heterogeneous catalysts, *J. Phys.: Condens. Matter* 15 (2003) R31–R62.
- [4] A.A. Serga, A.V. Chumak, A. Andre, G.A. Melkov, A.N. Slavin, S.O. Demokritov, B. Hillebrands, Parametrically Stimulated Recovery of a Microwave Signal Stored in Standing Spin-Wave Modes of a Magnetic Film, *Phys. Rev. Lett.* 99 (2007) 227202.
- [5] K. Lee, S. Kim, Control of spin-wave phase and wavelength by electric current on the microscopic scale, *J. Appl. Phys.* 104 (2008) 053909.
- [6] L. Bogani, W. Wernsdorfer, Molecular spintronics using single-molecule magnets, *Nat. Mater.* 7 (2008) 179.
- [7] T. Balashov, A.F. Takács, W. Wulfhekel, J. Kirschner, Magnon Excitation with Spin-Polarized Scanning Tunneling Microscopy, *Phys. Rev. Lett.* 97 (2006) 187201.
- [8] B. Bourahla, A. Khater, R. Tigrine, R. O. M.A. Ghantous, Magnon coherent conduction via atomic nanocontacts, *J. Phys.: Cond. Matter* 19 (2007) 266208.
- [9] A. Khater, B. Bourahla, M.A. Ghantous, R. Tigrine, R. Chadli, Magnons coherent transmission and heat transport at ultrathin insulating ferromagnetic nanojunctions, *J. Eur. Phys. B* 82 (2011) 53.
- [10] D. Ghader, V. Ashokan, A. Khater, M.A. Ghantous, Spin waves transport across a ferrimagnetically ordered nanojunction of cobalt-gadolinium alloy between cobalt leads, *Eur. Phys. J. B* 86 (2013) 180-1.
- [11] R. Tigrine, A. Khater, M. Boucherrab, B. Bourahla, R. Chadli, S. Amoudache, Spin Waves Dynamics at Disordered Soliton Boundaries, *Quantum Matter* 3 (2014) 542.
- [12] B. Bourahla, O. Nafa, A. Khater, Spin Wave Transmission by Spin Impurities in a Quasi-1D Heisenberg Ferromagnetic Tubular Structure, *J. Superconductivity and Novel Mag.:* Springer Science, 28, 2015, p. 1843.
- [13] V.V. Kruglyak, S.O. Demokritov, D. Grundler, Magnonics, *J. Phys. D Appl. Phys.* 43 (2010) 264001.
- [14] K. Vogt, F.Y. Fradin, J.E. Pearson, T. Sebastian, S.D. Bader, B. Hillebrands, A. Hoffmann, H. Schultheiss, Realization of a spin-wave multiplexer, *Nat. Commun.* 5 (2014) 3727.
- [15] S. Wintz, V. Tiberkevich, M. Weigand, J. Raabe, J. Lindner, A. Erbe, A. Slavin, J. Fassbender, Magnetic vortex cores as tunable spin-wave emitters, *Nature Nanotechnol.* 11 (2016) 948.
- [16] M.A. Ghantous, A. Khater, D. Ghader, V. Ashokan, Sublattice magnetizations of ultrathin alloy $[\text{Co}_{1-c}\text{Gd}_c]_n[\text{Co}_{1-c}\text{Gd}_c]_n$ nanojunctions between Co leads using the combined effective field theory and mean field theory methods, *J. Appl. Phys.* 113 (2013) 094303.
- [17] V. Ashokan, M.A. Ghantous, A. Khater, Modeling the sublattice magnetizations for the layered bcc nanojunction $\dots\text{Fe}[\text{Fe}_{1-c}\text{Co}_c]_l\text{Fe}\dots$ systems, *J. Mag. Mag. Mat.* 396 (2015) 16.
- [18] V. Ashokan, M.A. Ghantous, D. Ghader, A. Khater, Computation of magnons ballistic transport across an ordered magnetic iron-cobalt alloy nanojunction between iron leads, *Thin Solid Films* 616 (2016) 6.
- [19] B. Glaubitz, S. Buschhorn, F. Brüssing, R. Abrudan, H. Zabel, Development of magnetic moments in $\text{Fe}_{1-x}\text{Ni}_x$ alloys, *J. Phys.: Condens. Matter* 23 (2011) 254210.
- [20] S. Kumar, K. Roy, K. Maity, T.P. Sinha, D. Banerjee, K.C. Das, R. Bhattacharya, Superparamagnetic Behavior of Fe-Ni Alloys at Low Ni Concentration, *Phys. Stat. Sol. A* 167 (1998) 175.
- [21] C.W. Yang, D.B. Williams, J.I. Goldstein, A revision of the Fe-Ni phase diagram at low temperatures ($<400^\circ\text{C}$), *J. Phase Equil.* 17 (1996) 522.
- [22] V.V. Tcherdyntsev, S.D. Kaloshkin, I.A. Tomilin, E.V. Shelekov, Y.V. Baldokhin, Formation of iron-nickel nanocrystalline alloy by mechanical alloying, *Nanostruct. Mater.* 12 (1999) 139.
- [23] Y.V. Baldokhin, P.Y. Kolotykin, Y.I. Petrov, E.A. Shafranovsky, On the exhibition of high and low spin states of the fcc phase in ultrafine Fe and Fe-Ni particles, *Phys. Lett. A* 189 (1994) 137.
- [24] F.O. Schumann, R.F. Willis, K.G. Goodman, J.G. Tobin, Magnetic instability of ultrathin fcc $\text{Fe}_x\text{Ni}_{1-x}$ films, *Phys. Rev. Lett.* 79 (1997) 5166.
- [25] X.G. Li, A. Chiba, S. Takahashi, Preparation and magnetic properties of ultrafine particles of Fe-Ni alloys, *J. Magn. Magn. Mater.* 170 (1997) 339.
- [26] In: ASM Specialty Handbook: nickel, cobalt, and their alloys. [S.I.]: ASM International, 92–101 (2000).
- [27] M. Kläui, Head-to-head domain walls in magnetic nanostructures, *J. Phys.: Condens. Matter* 20 (2008) 313001.
- [28] J.-M. Yan, X.-B. Zhang, S. Han, H. Shioyama, Q. Xu, Magnetically recyclable Fe-Ni alloy catalyzed dehydrogenation of ammonia borane in aqueous solution under ambient atmosphere, *J. Power Sources* 194 (2009) 478–481.
- [29] J. Liu, K. Barmak, Interdiffusion in nanometric Fe/Ni multilayer films, *J. Vac. Sci. Technol.* 33 (2015) 021510.
- [30] F. Ay, B.Z. Rameev, A.C. Basaran, G.S. Kupriyanova, A.Y. Goikman, B. Aktaş, Magnetic Properties of Fe/Ni and Fe/Co Multilayer Thin Films, *Appl. Magn. Reson.* 48 (2017) 85.
- [31] L. Häggström, I. Soroka, S. Kamali, Thickness dependent crystallographic transition in Fe/Ni multilayers, *J. Phys.: Conf. Ser.* 217 (2010) 012112.
- [32] E.A. Moujaes, A. Khater, M.A. Ghantous, Combined analysis of ferromagnetic materials using the Heisenberg Green functions and Ising EFT methods, *J. Magn. Magn. Mater.* 391 (2015) 49.
- [33] T. Kaneyoshi, Spin glass ordering temperature beyond its mean field value, *J. Mag. Mat.* 119 (1980) 15.
- [34] R. Honmura, A. Khater, I.P. Fittipaldi, T. Kaneyoshi, Phase diagrams of mixed crystals - Ising models, *Solid St. Comm.* 41 (1982) 385.
- [35] A. Khater, G.L. Gal, T. Kaneyoshi, Phase diagram of a spin-12 bilayer system with disordered interfaces, *Physics Letters A* 171 (1992) 237.
- [36] M. Fresneau, A. Virlouvet, A. Khater, Calculation of the phase diagrams of ferromagnetic alloys A_xB_{1-c} and application to transition metal-rare-earth $\text{Fe}_x\text{Gd}_{1-c}$ and $\text{Fe}_x\text{Tb}_{1-c}$ materials, *J. Mag. Mag. Mat.* 202 (1999) 220.
- [37] A. Virlouvet, A. Khater, H. Aouchiche, O. Rafil, K. Maschke, Scattering of vibrational waves in perturbed two-dimensional multichannel asymmetric waveguides as on an isolated step, *Phys. Rev. B* 59 (1999) 4933.
- [38] A. Khater, M. Belhadi, Phonon scattering via an atomic well in free standing thin solid films, *Surf. Rev. Lett.* 16 (2009) 1.
- [39] M. Belhadi, A. Khater, J. Hardy, K. Maschke, Phonon transmission via a three-terminal junction in low dimensional wave-guides, *Eur. Phys. J. Appl. Phys.* 35 (2006) 185.
- [40] D. Szczesniak, A. Khater, Z. Bak, R. Szczesniak, M.A. Ghantous, Quantum conductance of silicon-doped carbon wire nanojunctions, *Nanoscale Research Letters* 7 (2012) 616.
- [41] V. Ashokan, M.A. Ghantous, D. Ghader, A. Khater, Ballistic transport of spin waves incident from cobalt leads across cobalt-gadolinium alloy nanojunctions, *J. Mag. and Mag. Mat.* 363 (2014) 66.
- [42] R. Landauer, Electrical resistance of disordered one-dimensional lattices, *Philos. Mag.* 21 (1970) 863.
- [43] M. Büttiker, Four-Terminal Phase-Coherent Conductance, *Phys. Rev. Lett.* 57 (1986) 1761.
- [44] P. Lilienfeld, Visualizing Rayleigh Scattering through UV Photography, *Opt. Photonics News.* 15 (2004) 32–39.
- [45] S. Chakraborti, Verification of the Rayleigh scattering cross section, *Am. J. Phys.* 75 (2007) 824–826.
- [46] Y.Y. Chuang, Y.A. Chang, R. Schmid, C.A. Hooley, Magnetization of ultrathin $[\text{Fe}_{1-c}\text{Ni}_c]_n$ alloy nanojunctions between Fe or Co leads using an Ising EFT-MFT model, arXiv: 1208.2850, 1–7 (2012).
- [47] E.A. Moujaes, M.A. Ghantous, Magnetic contributions to the thermodynamic functions of alloys and the phase equilibria of Fe-Ni system below 1200 K, *J. Magn. Magn. Mater.* 423 (2017) 359–372.
- [48] F. Liot, C.A. Hooley, Numerical Simulations of the Invar Effect in Fe-Ni, Fe-Pt, and Fe-Pd Ferromagnets. e-print arXiv: 1208.2850 1-7 (2012).
- [49] R.A. Reck, Local magnetic moments and g' in Fe-Ni alloys, *Phys. Rev. B* 9 (1974) 2381.
- [50] J.S. Kouvel, R.H. Wilson, Magnetization of Iron-Nickel Alloys Under Hydrostatic Pressure, *J. Appl. Phys.* 32 (1961) 435-41.
- [51] I.I. Yakimov, G.F. Torba, V.V. Litvintsev, Exchange interaction dependence on lattice parameter in iron-nickel alloys, *Fiz. Metallov i Metallovedenie* 47 (1) (1979) 67–71.
- [52] G.J. Johanson, M.B. McGirr, D.A. Wheeler, Determination of the Néel Temperature of Face-Centered-Cubic Iron, *Phys. Rev. B* 1 (1970) 3208.
- [53] P. Vargas, D. Altbir, Dipolar effects in multilayers with interface roughness, *Phys. Rev. B* 62 (2000) 6337.
- [54] A. Khater, B. Bourahla, M.A. Ghantous, R. Tigrine, R. Chadli, Magnons coherent transmission and heat transport at ultrathin insulating ferromagnetic nanojunctions, *Eur. Phys. J. B* 82 (2011) 53.
- [55] M.A. Ghantous, E.A. Moujaes, J.L. Dunn, A. Khater, Cooperative Jahn-Teller effect in a 2D mesoscopic C_{60}^n system with D_{3d} symmetry adsorbed on buffer layers using Ising EFT model, *Eur. Phys. J. B* 85 (2012) 178.
- [56] A. Khater, M.A. Ghantous, Calculation of spin modes on magnetic surface clusters, *Sur. Sci.* 498 (2002) L97.
- [57] G. Sclauzero, A.D. Corso, Efficient DFT+U calculations of ballistic electron transport: Application to Au monatomic chains with a CO impurity, *Phys. Rev. B* 87 (2013) 085108.
- [58] W. Neng-Ping, Electronic Transport Calculations Using Maximally-Localized Wannier Functions, *Commun. Theor. Phys.* 55 (2011) 158.
- [59] D. Szczesniak, A. Khater, Electronic conductance via atomic wires: a phase field matching theory approach, *Eur. Phys. J. B* 85 (2012) 174.
- [60] D.A. Rowlands, J.B. Staunton, B.L. Gyorffy, Korringa-Kohn-Rostoker nonlocal coherent-potential approximation, *Phys. Rev. B.* 67 (2003) 115109.